



1
2 DOCTORAL THESIS
3

4 Optimisation studies and background
5 estimation in searches for the supersymmetric
6 partner of the top quark in all-hadronic final
7 states with the ATLAS Detector at the LHC
8

9 A thesis submitted in fulfillment of the requirements
10 for the degree of Doctor of Philosophy

11 in the

12 Experimental Particle Physics Research Group
13 School of Mathematical and Physical Sciences

14 Author:
15 Fabrizio MIANO

Supervisor:
Dr. Fabrizio SALVATORE

12th October 2017

Dedicated to my family.

*Have no fear for atomic energy
'cause none of them can stop the
time*

17

Robert Nesta Marley

18

Acknowledgments

¹⁹ Thanks to every single thing that went wrong. It made me stronger.

Declaration

21 I, Fabrizio MIANO, hereby declare that this thesis, titled, "Optimisation studies and back-
22 ground estimation in searches for the supersymmetric partner of the top quark in all-
23 hadronic final states with the ATLAS Detector at the LHC" has not been and will not be,
24 submitted in whole or in part to another University for the award of any other degree.

25 *Brighton, June 2018*

27

University of Sussex

28

School of Mathematical and Physical Sciences

29

Experimental Particle Physics Research Group

30

Doctoral Thesis

31

32 Optimisation studies and background estimation in searches for
33 the supersymmetric partner of the top quark in all-hadronic final
34 states with the ATLAS Detector at the LHC

35

36

by Fabrizio MIANO

37

Abstract

38 This thesis presents searches for supersymmetry in $\sqrt{s} = 13$ TeV proton-proton collisions
39 at the LHC using data collected by the ATLAS detector in 2015, 2016 and 2017. Events
40 with 4 or more jets and missing transverse energy were selected. Kinematic variables
41 were investigated and optimisations were performed to increase the sensitivity to su-
42 persymmetric signals. Standard Model backgrounds were estimated by means of Monte
43 Carlo simulations and data-driven techniques. Before analysing the data in the blinded
44 signal regions the agreement between data and background predictions and the extrapol-
45 ations from control and validation regions to signal regions were validated. The analysis
46 yielded no significant excess in any of the analyses performed. Therefore limits were
47 set and the results were interpreted as lower bounds on the masses of supersymmetric
48 particles in various scenarios and models.

49

50

Contents51

52	Introduction	1
53	1 The Standard Model, Supersymmetry, and the motivations behind it	2
54	1.1 The Standard Model	2
55	1.1.1 Overview	3
56	1.1.2 Limitations of the Standard Model	5
57	1.2 Supersymmetry	5
58	1.2.1 Why SUSY?	5
59	1.2.2 Minimal Supersymmetric Standard Model	5
60	1.2.3 <i>R</i> -parity SUSY	5
61	1.2.4 Simplified models	5
62	1.2.5 Phenomenological MSSM	5
63	2 The ATLAS Experiment at the LHC	6
64	2.1 The LHC	6
65	2.2 The ATLAS Detector	9
66	2.2.1 The Magnet System	10
67	2.2.2 The Inner Detector	11
68	2.2.3 The Calorimeters	14
69	2.2.4 The Muon Spectrometer	16
70	2.3 The ATLAS Trigger System	17
71	2.3.1 Level 1 Trigger	18
72	2.3.2 High-Level Trigger	18

73	3 The <i>b</i>-jet Trigger Signature in ATLAS	20
74	3.1 Trigger Efficiency	20
75	4 Event Simulation and Reconstruction	21
76	4.1 Event Generation	21
77	4.1.1 Parton Distribution Functions (PDFs)	21
78	4.1.2 Matrix Element Calculation	21
79	4.1.3 Parton Showers	21
80	4.1.4 Hadronisation	21
81	4.2 Detector Simulation	22
82	5 Stop searches in final states with jets and missing transverse energy	23
83	6 Results and Statistical Intepretations	24
84	Trigger	25
85	Bibliography	26

86

87

List of Tables

88

89

1.1 Forces and mediators described by the SM	4
--	---

90

91

List of Figures

92

93	2.1	CERN Accelerator complex. The LHC is the last ring (dark grey line). Smaller machines are used for early-stage acceleration and also to provide beams for other experiments [1].	8
94	2.2	Cut-away view of the ATLAS detector. The dimensions of the detector are 25 m in height and 44 m in length. The overall weight of the detector is approximately 7000 tonnes [1].	9
95	2.3	The ATLAS magnet system.	11
96	2.4	The ATLAS Inner Detector	12
97	2.5	A computer generated image of the full calorimeter.	14
98	2.6	Cut-away view of the ATLAS muon system [2].	16
99	2.7	The ATLAS TDAQ system. L1Topo and FTK were being commissioned during 2015 and not used for the results shown in this thesis [3].	17
100			
101			
102			
103			
104			

105 _____

106 **Introduction**

107 _____

108 Last thing to write

109

CHAPTER 1

110

111 The Standard Model, Supersymmetry, and the motivations behind it

112

113

A theory is something nobody believes, except the person who made it. An experiment is something everybody believes, except the person who made it.

Albert Einstein

114 The Standard Model (SM) of particle physics is an effective theory that aims to provide
 115 a general description of fundamental particles and the phenomena we see in nature, i. e.
 116 the way they interact. Unfortunately, our understanding of nature is still limited due to
 117 some opened question to which the SM is not able to answer to, yet.

118 In this chapter, an overview of the SM will be presented in Section 1.1 together with
 119 the limitations of such theory and some of the reasons behind the need of an extension.
 120 For the last decades theoretical physicsts have been trying to provide extensions to the
 121 SM, the so-called beyond-the-SM theories. Among these, one of the most popular, Super-
 122 symmetry which will be discussed in Section 1.2.

123 **1.1 The Standard Model**

124 The 20th century can be considered a quantum revolution. Several experiments led to
 125 discoveries which were found to be, together with the formalised theory, a solid base of
 126 the Standard Model of particle physics and our description of nature. Several particles

¹²⁷ were predicted first by the SM and then experimentally observed e.g. the W and the Z
¹²⁸ bosons, the τ lepton, [4], and more recently the Higgs boson at the LHC discovered by
¹²⁹ ATLAS [5] and CMS [6].

¹³⁰ The SM lays on a Quantum Field Theory (QFT) where particles are treated like fields.
¹³¹ It can describe three of the four fundamental forces; weak, electromagnetic, and strong.
¹³² As of today, gravity is not considered in the SM. Sections 1.1.1 and 1.1.2 will be focused
¹³³ on the description of the fields together with the carriers of the information, and on the
¹³⁴ limitations that such theory implies, respectively.

¹³⁵ 1.1.1 Overview

¹³⁶ The most general classification of the particles within the SM can be made by means of
¹³⁷ spin. Fermions have half-integer spin values - and are usually referred to as matter -, and
¹³⁸ bosons have integer-spin values. A noteworthy subset of bosons is formed by the Spin-1
¹³⁹ bosons (also known as gauge bosons). These can be considered the information carriers
¹⁴⁰ or, in fact, the mediators of the forces.

¹⁴¹ Fermions

¹⁴² Six quarks and six leptons belong to the fermions family. In particular, fermions can be
¹⁴³ grouped into three generations. Each generation contains four particles; one up- and
¹⁴⁴ one down-type quark, one charged lepton and one neutral lepton. The masses of the
¹⁴⁵ charged leptons and quarks increase with the generation. The six quarks of the SM can
¹⁴⁶ be grouped into three doublets:

$$\begin{pmatrix} u \\ d \end{pmatrix}, \quad \begin{pmatrix} c \\ s \end{pmatrix}, \quad \begin{pmatrix} t \\ b \end{pmatrix}$$

¹⁴⁷ The up-type quarks (up, charm, top) have charge $+\frac{2}{3}e$ and the down-type quarks (down,
¹⁴⁸ strange, beauty/bottom) have charge $-\frac{1}{3}e$, where e is the electron charge. Quarks also
¹⁴⁹ have another quantum number that can be seen as the analogue of the electric charge,
¹⁵⁰ which is the colour charge. This can exist in three different states; "red", "green" and
¹⁵¹ "blue". Moreover, as a consequence of *confinement*, which will be discussed later on in
¹⁵² this section, quarks cannot exist as free particles. They rather group to form hadronic
¹⁵³ matter, also known as *hadrons*. There are two kinds of hadrons; mesons and baryons.
¹⁵⁴ Mesons are quark-antiquark systems, e.g. the pion, and baryons are three-quark system,

¹⁵⁵ e.g. protons and neutrons. Quarks and anti-quarks have a baryon number of $\frac{1}{3}$ and $-\frac{1}{3}$,
¹⁵⁶ respectively.

¹⁵⁷ There are six leptons and they can be classified in charged leptons (electron e , muon
¹⁵⁸ μ , tau τ) and neutral leptons (electron neutrino ν_e , muon neutrino ν_μ , tau neutrino ν_τ).

$$\begin{pmatrix} \nu_e \\ e^- \end{pmatrix}, \quad \begin{pmatrix} \nu_\mu \\ \mu^- \end{pmatrix}, \quad \begin{pmatrix} \nu_\tau \\ \tau^- \end{pmatrix}$$

¹⁵⁹ Each lepton has a characteristic quantum number, called lepton number (L). Negatively
¹⁶⁰ (positively) charged leptons have $L = -1$ ($L = 1$) and neutral leptons have $L = 0$. The
¹⁶¹ lepton number is conserved in all the interactions.

¹⁶² Forces of Nature

¹⁶³ Forces in the SM are described by gauge theories, where the interactions is mediated by a
¹⁶⁴ vector gauge boson. The electromagnetic force is described by Quantum ElectroDynam-
¹⁶⁵ ics (QED) and, as its mediator is the photon (γ) which couples to charged particles, it only
¹⁶⁶ affects charged leptons and quarks, whereas neutrinos cannot. They are instead affected
¹⁶⁷ by the weak force which is mediated by the bosons W^\pm and Z^0 . The weak interaction is
¹⁶⁸ associated with handedness (the projection of a particle spin onto its direction of motion).
¹⁶⁹ Both leptons and quarks have left- and right-handed components. However, only the
¹⁷⁰ left-handed (right-handed) component for neutrinos (anti-neutrinos) has been observed.
¹⁷¹ This means that nature prefers to produce left-handed neutrinos and right-handed anti-
¹⁷² neutrinos, which is the so-called parity violation. The strong interactions, mediated by
¹⁷³ the gluon (electrically neutral and massless), is described by Quantum ChromoDynamics
¹⁷⁴ (QCD). Table 1.1 summarises the forces described in the SM and their mediators' main
¹⁷⁵ characteristics. Finally, the gravitational force, which is believed to be mediated by the
¹⁷⁶ graviton, is not included in Table 1.1 as it is not part of the SM.

Table 1.1: Forces and mediators described by the SM

Force	Name	Symbol	Mass [GeV]	Charge
Electromagnetic	Photon	γ	0	0
Weak	W	W^\pm	80.398	$\pm e$
	Z	Z^0	91.188	0
Strong	Gluon	g	0	0

¹⁷⁷ In 1979 Sheldon Glashow, Abdus Salam, and Steven Weinberg were awarded the Nobel Prize in Physics for their contributions to the so-called electroweak unification. Weak
¹⁷⁸ and electromagnetic interactions were now unified. Quarks that interact through weak
¹⁷⁹ interaction are mixtures of SM eigenstates as described by the CKM matrix [7].
¹⁸⁰

¹⁸¹ **Gauge Groups**

¹⁸² **Electroweak Symmetry Breaking and the Higgs mechanism**

¹⁸³ **1.1.2 Limitations of the Standard Model**

¹⁸⁴ **1.2 Supersymmetry**

¹⁸⁵ **1.2.1 Why SUSY?**

¹⁸⁶ **1.2.2 Minimal Supersymmetric Standard Model**

¹⁸⁷ **1.2.3 *R*-parity SUSY**

¹⁸⁸ **1.2.4 Simplified models**

¹⁸⁹ **1.2.5 Phenomenological MSSM**

CHAPTER 2

190

191

192

The ATLAS Experiment at the LHC

193

194 ATLAS (A Toroidal LHC ApparatuS) is one of the four main experiments (ATLAS, CMS,
 195 ALICE, LHCb) taking data at a center-of-mass energy of 13 TeV using beams delivered by
 196 the Large Hadron Collider (LHC). In this chapter an overview of the LHC will be given
 197 in Section 2.1, then the ATLAS detector will be described in Section 2.2, and finally the
 198 Trigger system, used to cleverly store the data, will be described in Section 2.3. A more
 199 in-depth description of the Trigger algorithms I have been involved in will be given in
 200 Chapter 3.

2.1 The LHC

201 As of today, the LHC is the world's largest and most powerful particle accelerator. It
 202 was designed to help answer some of the fundamental open questions in particle phys-
 203 ics by colliding protons at an unprecedented energy and luminosity. It is located at the
 204 European Organisation for Nuclear Research (CERN), in the Geneva area, at a depth ran-
 205 ging from 50 to 175 metres underground. It consists of a 27-kilometre ring made of su-
 206 perconducting magnets, and inside it two high-energy particle beams travel in opposite
 207 directions and in separate beam pipes.

208 The beams are guided around the ring by a strong magnetic field generated by coils -
 209 made of special electric cables - that can operate in a superconducting regime. 1232 super-
 210 conducting dipole and 392 quadrupole magnets, with an average magnetic field of 8.3 T,
 211 are employed and kept at a temperature below 1.7 K, in order to preserve their supercon-

²¹³ ducting properties. The formers are used to bend the beams and the latters to keep them
²¹⁴ focused while they get accelerated.

²¹⁵ The collider first went live on September 2008 even though, due to a magnet quench
²¹⁶ incident that damaged over 50 superconducting magnets, it has been operational since
²¹⁷ November 2009 when low-energy beams circulated in the tunnel for the first time since
²¹⁸ the incident. This also marked the start of the main research programme and the begin-
²¹⁹ ning of the so-called Run 1: first operational run (2009 - 2013).

²²⁰ Performance of the LHC

²²¹ In June 2015 the LHC restarted delivering physics data, after a two-year break, the so-
²²² called Long Shutdown 1 (LS1), during which the magnets were upgraded to handle the
²²³ current required to circulate 7-TeV beams. It was the beginning of the so-called Run 2 -
²²⁴ second operational run (2015-2018) - during which LHC has collided up to 10^{11} bunches
²²⁵ of protons every 25 ns at the design luminosity - the highest luminosity the detector was
²²⁶ designed to cope with - of $2 \cdot 10^{34} \text{ cm}^{-2} \text{s}^{-1}$. The definition of the luminosity is:

$$\mathcal{L} = f \frac{n_b N_1 N_2}{4\pi\sigma_x\sigma_y} \quad (2.1)$$

²²⁷ where N_1 and N_2 are the number of protons per bunch in each of the colliding beams, f
²²⁸ is the revolution frequency of the bunch collisions, n_b the number of proton per bunch,
²²⁹ and σ_x and σ_y are the horizontal and vertical dimensions of the beam. The luminosity is
²³⁰ strictly related to the number of collisions occurring during a certain experiment via the
²³¹ following:

$$\mathcal{N}_{\text{event}} = \mathcal{L}\sigma_{\text{event}} \quad (2.2)$$

²³² where σ_{event} is the cross section of the process under investigation. It has not only collided
²³³ protons but also heavy ions, in particular lead nuclei at $\sqrt{s_{NN}} = 5.02 \text{ TeV}$, at a luminosity
²³⁴ of $10^{27} \text{ cm}^{-2} \text{s}^{-1}$ [8].

²³⁵ Acceleration stages

²³⁶ Before reaching the maximum energy, the proton beams are accelerated by smaller ac-
²³⁷ celerators through various stages. Figure 2.1 shows a sketch of the CERN's accelerator
²³⁸ complex. It all begins at the linear accelerator LINAC 2. Here protons are accelerated up
²³⁹ to 50 MeV, and then injected in the Proton Synchrotron Booster (PSB) where they reach
²⁴⁰ 1.4 GeV. The next stage is the Proton Synchrotron (PS), which boosts the beams up to 25

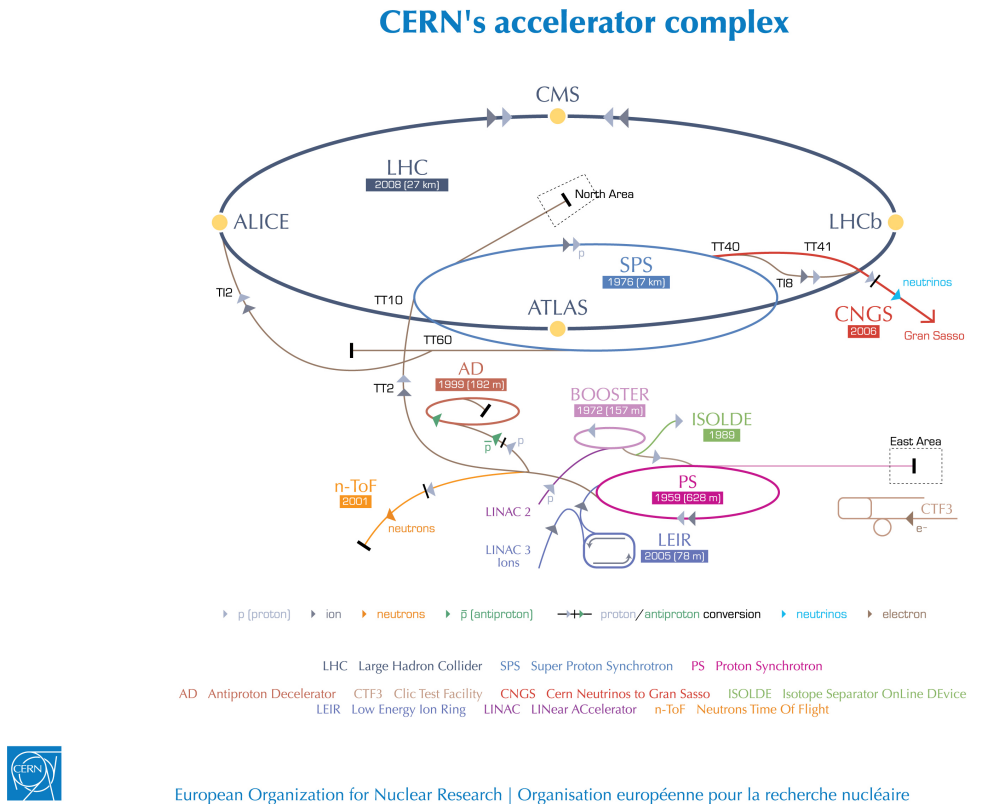


Figure 2.1: CERN Accelerator complex. The LHC is the last ring (dark grey line). Smaller machines are used for early-stage acceleration and also to provide beams for other experiments [1].

241 GeV and then the Super Proton Synchrotron (SPS) makes them reach energies up to 450
 242 GeV. Eventually, the beams are injected in bunches with a 25 ns spacing into the LHC,
 243 where they travel in opposite directions, while they are accelerated to up to 13 TeV. Once
 244 the bunches reach the maximum energy, they are made collide at four different points,
 245 inside four experiments around the ring [9].

246 The heavy ion beams acceleration procedure is slightly different. Their journey starts
 247 at LINAC 3 first, and the Low Energy Ion Ring (LEIR) then, before they make their way
 248 into the PS where they follow the same path as the protons [9].

249 The four large detectors on the collision points are; the multi-purpose detectors A Tor-
 250 oidal LHC ApparatuS (ATLAS), and Compact Muon Solenoid (CMS) [10], Large Hadron
 251 Collider beauty (LHCb) [11], which focuses on flavour physics, and A Large Ion Collider
 252 Experiment (ALICE) [12] which specialises in heavy ion physics. The *big four* are not the
 253 only experiments at the CERN's accelerator complex. There also are smaller experiments
 254 based at the the four caverns about the collision points e.g. TOTEM, LHCf and MoEDAL,
 255 but this will not be discussed any further in this thesis.

256 **2.2 The ATLAS Detector**

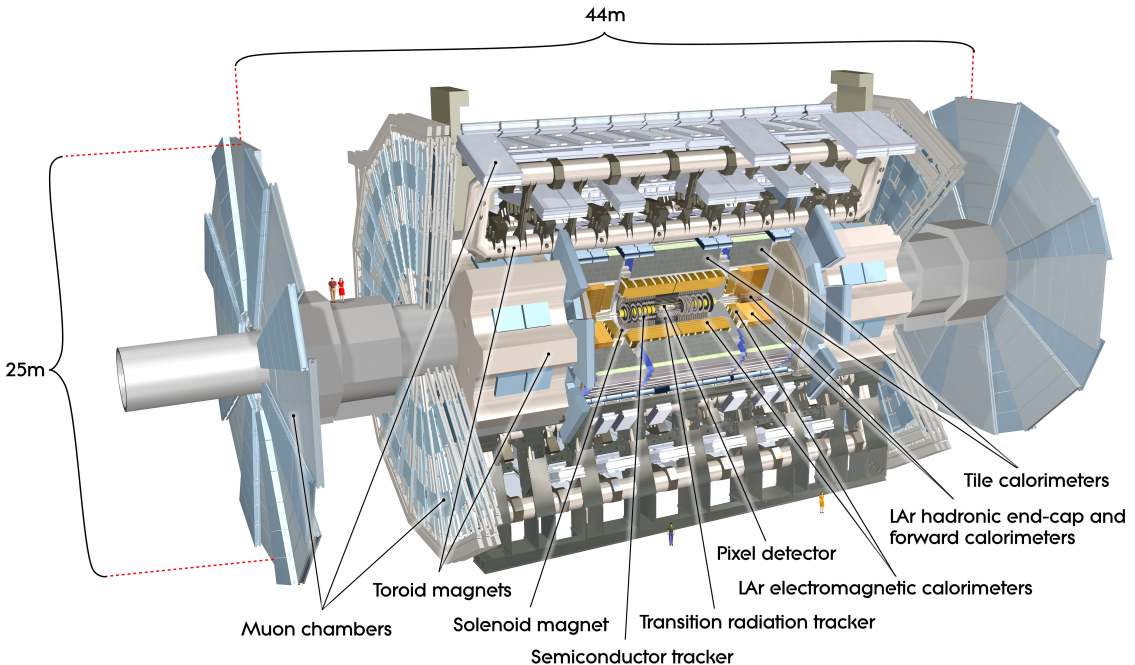


Figure 2.2: Cut-away view of the ATLAS detector. The dimensions of the detector are 25 m in height and 44 m in length. The overall weight of the detector is approximately 7000 tonnes [1].

257 ATLAS is a general-purpose detector designed to collect data with the highest luminosity provided by the LHC. It is located at CERN’s Point 1 cavern and it measures about 258 45 m in length and 25 m in diameter. It has a forward-backward symmetric cylindrical 259 geometry with respect to the interaction point and it is designed to reconstruct and measure 260 physics objects such as electrons, muons, photons and hadronic jets. Its design was 261 optimised to be as sensitive as possible to the discovery of the Higgs boson and beyond-262 the-Standard-Model (BSM) physics. In fact, thanks to the other sub-systems, ATLAS is 263 able to observe all possible decay products by covering nearly 4π steradians of solid 264 angle.

265 In Figure 2.2 a cut-away view of ATLAS with all its components is shown. The innermost layer is the Inner Detector (ID) which is the core of the tracking system and consists 266 of a Pixel, a Silicon micro-strip tracker (SCT), and a Transition Radiation Tracker (TRT). 267 It is submerged in a 2 T magnetic field, generated by a thin superconducting solenoid, 268 which bends all the charged particles’ trajectories allowing transverse momentum measurement. The electromagnetic and hadronic calorimeters form the next layer and they are 269 both used to perform precise energy measurements of photons, electrons, and hadronic 270 271 272

²⁷³ jets. Finally, the outermost layer corresponds to the Muon Spectrometer (MS) which, to-
²⁷⁴ gether with the ID, enclosed in a toroidal magnetic field, allows precise measurement of
²⁷⁵ momentum and position of muons. These sub-detectors will be discussed in more detail
²⁷⁶ in the following sections.

²⁷⁷ The ATLAS coordinate system

²⁷⁸ A coordinate system is taken on for the spatial definition of the sub-systems and kin-
²⁷⁹ ematic measurement of physics processes. Such system is defined starting from the in-
²⁸⁰ teraction point, defined as the origin. The z -axis is defined by the beam direction and the
²⁸¹ $x - y$ plan, as transverse to the beam direction.

²⁸² A quantity, known as pseudorapidity, (η), is defined to describe the angle of a particle
²⁸³ coming out of the collision, with respect to the beam axis:

$$\eta \equiv -\ln(\tan(\theta/2))$$

²⁸⁴ Here θ is the polar angle. The azimuthal angle, ϕ , is defined around the beam axis and
²⁸⁵ the polar angle. In the (η, ϕ) space a distance ΔR can be therefore defined as

$$\Delta R = \sqrt{\Delta\eta^2 + \Delta\phi^2}$$

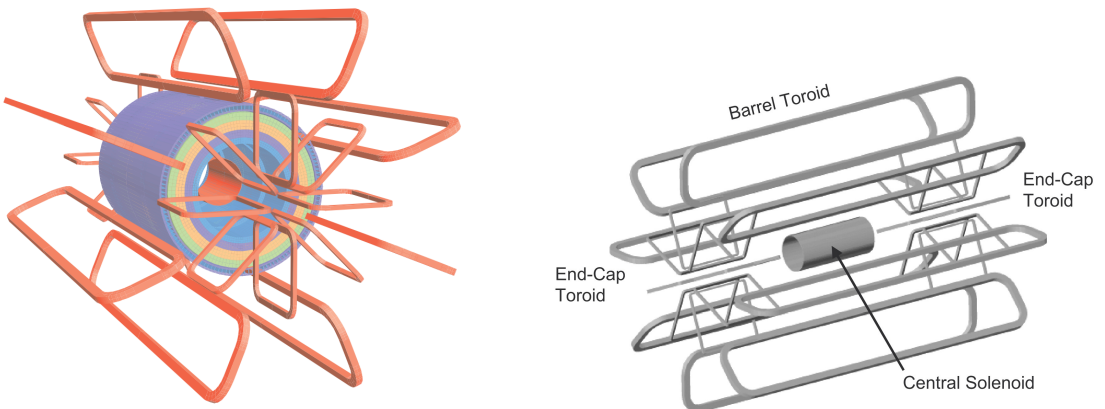
²⁸⁶ where $\Delta\eta$ and $\Delta\phi$ are the differences in pseudorapidity and azimuthal angle between
²⁸⁷ any two considered objects. A central and a forward region of pseudorapidity are also
²⁸⁸ defined such that the detector components are described as part of the *barrel* if they belong
²⁸⁹ to the former or as part of the *end-caps* if they belong to the latter.

²⁹⁰ 2.2.1 The Magnet System

²⁹¹ The ATLAS magnet system, 26 m long with a 22 m diameter, generates the magnetic
²⁹² field needed to bend the trajectories of charged particles in order to perform momentum
²⁹³ measurement. Figure 2.3a and 2.3b show the geometry of the system and its compo-
²⁹⁴ nents, which are made of NbTi - superconducting material - and will be described in the
²⁹⁵ following paragraphs.

²⁹⁶ The Central Solenoid

²⁹⁷ With an axial length of 5.8 m, an inner radius of 2.46 m, and an outer radius of 2.56 m, the
²⁹⁸ central solenoid magnet is located between the ID and the ECAL. Its function is to bend



(a) Geometry of magnet windings and tile calorimeter steel. The eight barrel toroid coils, with the end-cap coils interleaved are visible. The solenoid winding lies inside the calorimeter volume [2].

(b) Schematic view of the superconducting magnets [13].

Figure 2.3: The ATLAS magnet system.

299 the charged particles that go through the ID and it is aligned on the beam axis providing
 300 a 2 T axial magnetic field that allows accurate momentum measurement up to 100 GeV
 301 [13].

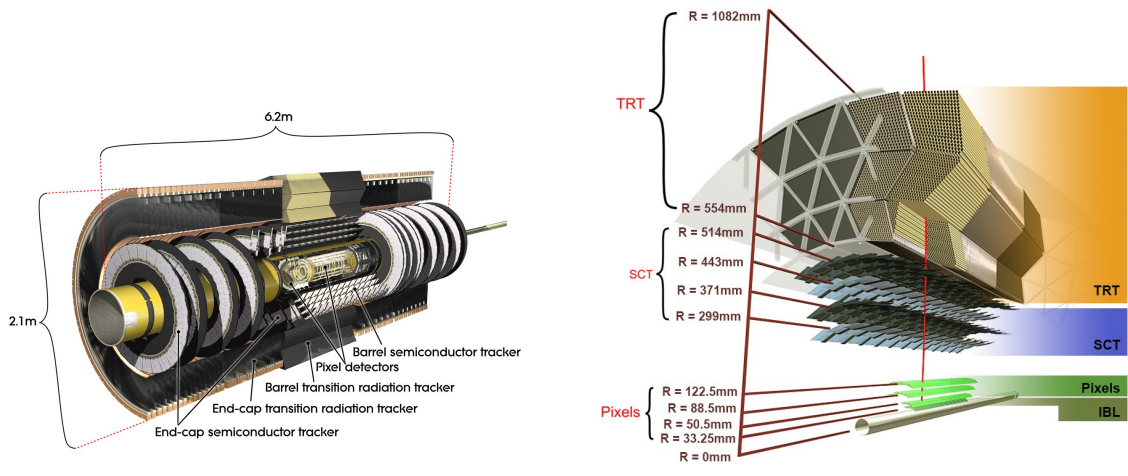
302 **The Barrel and the End-cap Toroids**

303 Figure 2.3b displays the toroid magnetic system that surrounds the calorimeters. With
 304 its cylindrical shape this component consists of a barrel and two end-caps toroids, each
 305 with eight superconducting coils. The system allows accurate measurement of muon
 306 momenta using a magnetic field of approximately 0.5 T (barrel) for the central regions
 307 and 1 T (end-cap) for the end-cap regions, respectively, which bends the particles in the
 308 θ direction.

309 **2.2.2 The Inner Detector**

310 The Inner Detector (ID) [14] is the innermost component of the ATLAS detector i. e. the
 311 nearest sub-detector to the interaction region and it is used to reconstruct charged particle
 312 tracks used in the selection of physics objects. In fact, it allows robust track reconstruc-
 313 tion, with accurate impact parameter resolution ($\sim 20\mu m$) and precise primary and sec-
 314 ondary vertex reconstruction for charged particles (tracks) above 500 MeV and within
 315 $|\eta| < 2.5$.

316 The ID is comprised of independent and concentric sub-systems, which are all shown



(a) Overview of the ATLAS ID with labels and dimensions.

(b) Diagram of the ATLAS ID and its sub-detectors.

Figure 2.4: The ATLAS Inner Detector

³¹⁷ in Figure 2.4:

- ³¹⁸ • Insertable B-Layer (IBL):

³¹⁹ innermost Pixel Detector layer added during ATLAS Run-2 upgrade (2013/2014)
³²⁰ to improve vertexing and impact parameter reconstruction;

- ³²¹ • Silicon Pixel Tracker (Pixel):

³²² made of silicon pixel layers and used mainly for reconstructing both the primary
³²³ and secondary vertices in an event;

- ³²⁴ • SemiConductor Tracker (SCT):

³²⁵ comprised of silicon microstrip layers; thanks to its resolution ($17 \times 580 \mu\text{m}$) it can
³²⁶ accurately measure particle momenta;

- ³²⁷ • Transition Radiation Tracker (TRT):

³²⁸ final layer comprised of various layers of gaseous straw tube elements surrounded
³²⁹ by transition radiation material.

³³⁰ These sub-detectors will be discussed in the following sections.

³³¹ **IBL**

³³² The IBL [15] is the innermost Pixel Detector layer as shown in Figure 2.4b. It is comprised
³³³ of 6M channels and each pixel measures $50 \times 250 \mu\text{m}$. Its resolution is $8 \times 40 \mu\text{m}$, The
³³⁴ addition of this new layer brought a considerable improvement on the performance of the

³³⁵ Pixel Detector by enhancing the quality of impact parameter reconstruction of tracks. In
³³⁶ particular, this was achieved by improving the vertex finding efficiency and the tagging
³³⁷ of bottom-quark-initiated jets (*b*-jets) which, in case of a B-layer failure, can be restored
³³⁸ by the IBL. Besides these improvements, the IBL insertion allowed ATLAS to better cope
³³⁹ with high luminosity effects such as the increase in event pile-up, which leads to high
³⁴⁰ occupancy and read-out inefficiency.

³⁴¹ **Pixel**

³⁴² The Pixel detector is comprised of 1750 identical sensorchip-hybrid modules, each cover-
³⁴³ ing an active area of 16.4×60.8 mm. The total number of modules correspond to roughly
³⁴⁴ 80 million semiconductor silicon pixels. The nominal pixel size is $50 \mu\text{m}$ in the ϕ direction
³⁴⁵ and $400 \mu\text{m}$ in the barrel region, along the z -axis (beam axis) [16]. The reason why such a
³⁴⁶ large amount of pixels is employed is justified by the need to cope with the high lumino-
³⁴⁷ sity in ATLAS. The silicon pixel detector measures 48.4 cm in diameter and 6.2 m in length
³⁴⁸ providing a pseudorapidity coverage of $|\eta| < 2.5$. Figure 2.4b shows the three concentric
³⁴⁹ barrel layers placed at 50.5 mm, 88.5 mm and 122.5 mm respectively. Furthermore, the
³⁵⁰ Pixel detector is made of six disk layers, three for each forward region, such that when a
³⁵¹ charged particle crosses the layers it will generate a signal at least in three space points.
³⁵² The fine granularity of such detector allows accurate measurement and precise vertex
³⁵³ reconstruction, as it provides a more accurate position measurement as a large detection
³⁵⁴ area is available. In particular, it has a resolution of $10 \times 115 \mu\text{m}$.

³⁵⁵ **SCT**

³⁵⁶ The SCT is made of 4088 modules of silicon micro-strip detectors arranged in four con-
³⁵⁷ centric barrel layers. It is mainly used for precise momentum reconstruction over a range
³⁵⁸ $|\eta| < 2.5$ and it was designed for precision measurement of the position using four points
³⁵⁹ (corresponding to eight silicon layers), obtained as track hits when crossing the layers.
³⁶⁰ Figure 2.4b shows the structure of the SCT with its four concentric barrel layers with
³⁶¹ radii ranging from 299 mm to 514 mm and two end-cap layers. Each module has an in-
³⁶² trinsic resolution of $17 \mu\text{m}$ in the $R - \phi$ direction and $580 \mu\text{m}$ in the z direction. As the
³⁶³ SCT is further away from the beam-pipe than the Pixel detector, it has to cope with re-
³⁶⁴ duced particle density. This allows for reduced granularity maintaining the same level of
³⁶⁵ performance of the Pixel detector: SCT can use ~ 6.3 million read-out channels.

366 **TRT**

367 The last and outermost of the sub-systems in the ID is the TRT. It is a gaseous detector
368 which consists of 4 mm diameter straw tubes wound from a multilayer film reinforced
369 with carbon fibers and containing a 30 μm gold plated tungsten wire in the center. The
370 straw is filled with a gas mixture of 70% Xe, 27% CO₂ and 3% O₂ [17]. As shown in Fig-
371 ure 2.4b, its section consists of three concentric layers with radii ranging from 544 mm to
372 1082 mm, each of which has 32 modules containing approximately 50,000 straws, 1.44 m
373 in length, aligned parallel to the beam direction with independent read-out at both ends.
374 Both end-cap sections are divided into 14 wheels, with roughly 320,000 straws in the
375 R-direction. The average 36 hits per track in the central region of the TRT allow continu-
376 ous tracking to enhance pattern recognition and momentum resolution in the $|\eta| < 2.5$
377 region. It also improves the p_{T} resolution for longer tracks.

378 **2.2.3 The Calorimeters**

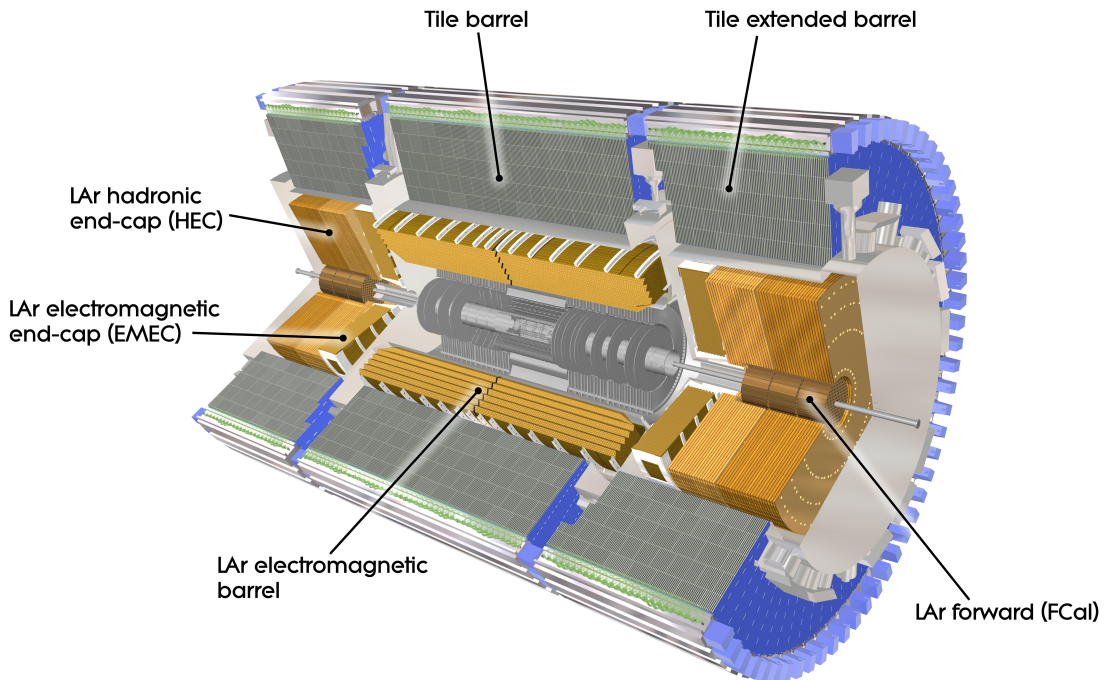


Figure 2.5: A computer generated image of the full calorimeter.

379 The ATLAS Calorimeter system, shown in Figure 2.5, is comprised of two main sub-
380 systems; the electromagnetic calorimeter (ECAL) and hadronic calorimeter (HCAL), which
381 are designed to stop and measure the energy of electromagnetic-interacting and had-

³⁸² ronic particles respectively. The combination of the two provides full coverage in ϕ and
³⁸³ $|\eta| < 4.95$. Particles slow down and lose energy generating showers when crossing dif-
³⁸⁴ ferent layers. The ECAL is comprised of one barrel and two end-cap sectors employing
³⁸⁵ liquid Argon (LAr). The showers hereby develop as electrons pairs which are then col-
³⁸⁶ lected. The HCAL is also comprised of one barrel and two end-cap sectors. The sensors
³⁸⁷ in the barrel of the HCAL are tiles of scintillating plastic whereas LAr is employed for
³⁸⁸ the end-cap. A forward region, the closest possible to the beam, is covered by a LAr for-
³⁸⁹ ward calorimeter (FCal). The LAr and Tile Calorimeter will be briefly discussed in the
³⁹⁰ following paragraphs.

³⁹¹ **The Liquid Argon Calorimeters**

³⁹² The ECAL is comprised of multiple layers of liquid Argon (LAr) sampler and lead ab-
³⁹³ sorber. The choice of its accordion-geometry design brought two main advantages; full
³⁹⁴ ϕ coverage with no non-interactive regions (no cracks); fast extraction of signals coming
³⁹⁵ from both front or rear end of the electrodes. It is made of two half-barrel wheels, both
³⁹⁶ placed in the barrel cryostat, that provide a pseudorapidity coverage up to $|\eta| < 1.475$
³⁹⁷ and two end-cap detectors providing $1.375 \leq |\eta| \leq 3.20$ coverage in two end-cap cryo-
³⁹⁸ stats. The junction between the barrel and end cap components defines the crack region
³⁹⁹ and any signal coming from the crack region is therefore discarded.

⁴⁰⁰ In the $|\eta| < 1.8$ region there is an additional layer, placed at the front of the calori-
⁴⁰¹ meter, that is made of a thin (0.5 cm in the end-cap and 1.1 cm in the barrel) LAr layer
⁴⁰² with no absorber [18]. This additional layer was designed to correct for the energy lost,
⁴⁰³ as particles enter the calorimeter, by taking a measurement just before the majority of the
⁴⁰⁴ electromagnetic shower is developed.

⁴⁰⁵ **The Tile calorimeter**

⁴⁰⁶ The main purpose of the hadronic calorimeter is to measure the energy of hadronic
⁴⁰⁷ showers. It is built employing steel and scintillating tiles coupled to optical fibres which
⁴⁰⁸ are read out by photo-multipliers. As shown in Figure 2.5, the HCAL is made up of three
⁴⁰⁹ cylinders; a central barrel, 5.64 m long covering a region $|\eta| < 1.0$, and two extended
⁴¹⁰ barrel, 2.91 m long covering a reigon $0.8 < |\eta| < 1.7$. Each cylinder is made up of 64
⁴¹¹ modules and each module is in turn made up of three layers. Ultimately, the smallest
⁴¹² section of the calorimeter module is a cell with a $\Delta\phi \times \Delta\eta = 0.1 \times 0.1$ granularity for the
⁴¹³ two innermost layers and $\Delta\phi \times \Delta\eta = 0.2 \times 0.1$ for the outermost one.

414 2.2.4 The Muon Spectrometer

415 The MS [19], shown in Figure 2.6, is the outermost sub-system of the whole ATLAS de-
 416 tector. As such, it surrounds the calorimeters and its main function is to perform precision
 417 measurement of muons momenta. The deflection of muon tracks employing large super-
 418 conducting air-core toroid magnets and high-precision tracking chambers is at the heart
 419 of such high precision measurement.

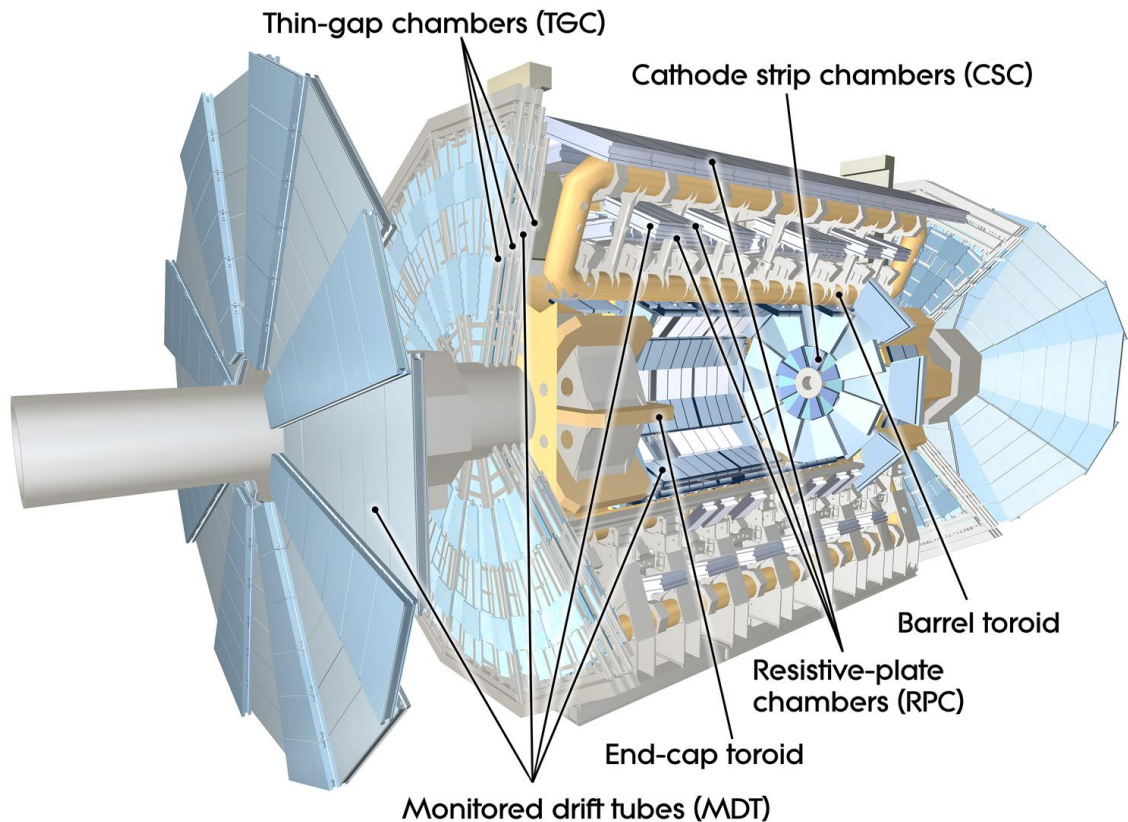


Figure 2.6: Cut-away view of the ATLAS muon system [2].

420 The MS is comprised of one large barrel toroid, covering the region $|\eta| \leq 1.4$, and two
 421 end-cap toroids, covering $1.6 < |\eta| \leq 2.7$ which are employed together to achieve the
 422 track-bending effect wanted. The magnitude of the magnetic field in the barrel, generated
 423 by eight large superconducting coils, ranges from 0.5 to 2 T.

424 Around the beam axis, three cylindrical layers make way for the chambers, placed in
 425 planes perpendicular to the beam, used to measure tracks.

426 Monitored Drift Chambers (MDTs) are employed over most of the pseudorapidity
 427 range to provide precision measurement of track coordinates in the bending direction.
 428 Cathode Strip Chambers (CSCs) are instead employed at large pseudorapidity ($2 < |\eta| <$
 429 2.7). Finally, in the end-cap regions Thin-Gap Chambers (TGCs) together with Resistive-

⁴³⁰ Plate Chambers (RPCs) are dedicated to the Trigger System discussed in Section 2.3.

⁴³¹ 2.3 The ATLAS Trigger System

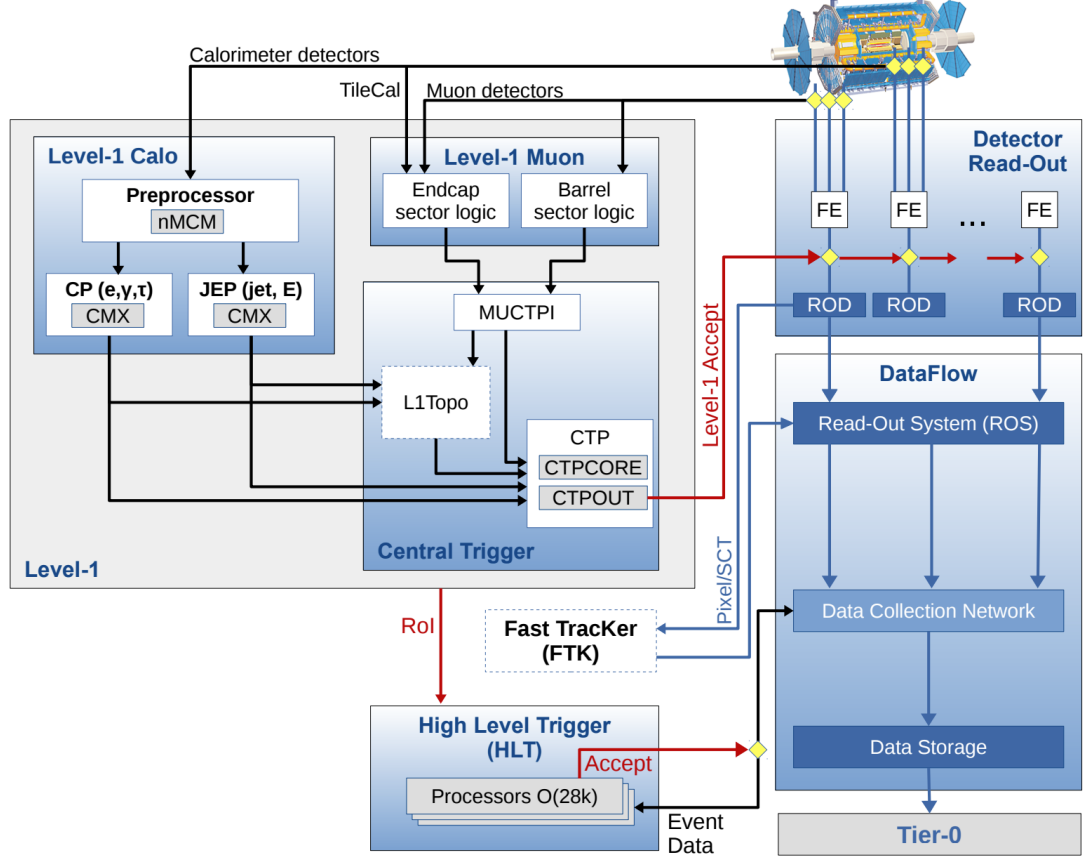


Figure 2.7: The ATLAS TDAQ system. L1Topo and FTK were being commissioned during 2015 and not used for the results shown in this thesis [3].

⁴³² The ATLAS Trigger System is at the heart of data taking. It is an essential component
⁴³³ of any nuclear or particle physics experiment since it is responsible for deciding whether
⁴³⁴ or not to store an event for later study [3]. The ATLAS Trigger system is employed to
⁴³⁵ reduce the event rate from ~ 40 MHz¹ bunch-crossing² to ~ 200 Hz which corresponds
⁴³⁶ to roughly 300 MB/s.

⁴³⁷ The Trigger and Data Acquisition (TDAQ) system shown in Figure 2.7 consists of
⁴³⁸ a hardware-based first level trigger (L1) and a software-based high-level trigger (HLT).
⁴³⁹ The L1 trigger decision is formed by the Central Trigger Processor (CTP), which receives

¹The LHC delivers beams with a bunch-spacing of 25 ns.

²The term bunch-crossing is hereby used when referring to a collision between two bunches of protons. Since only a certain fraction of the total momentum carried by each proton contributes to the collision, an average number of interactions per bunch-crossing, $\langle \mu \rangle$ is used.

⁴⁴⁰ inputs from the L1 calorimeter (L1Calo) and L1 muon (L1Muon) triggers. The first level
⁴⁴¹ (L1), which was designed to perform the first selection step, is a hardware-based system
⁴⁴² that uses information from the calorimeter and muon subdetectors. It also defines the so-
⁴⁴³ called Regions of Interest (RoIs) within the detector to be investigated by the next level
⁴⁴⁴ trigger, the HLT. Additionally, a Fast TracKer (FTK) system [20] (not yet installed) will
⁴⁴⁵ provide global ID track reconstruction at the L1 trigger rate using lookup tables stored
⁴⁴⁶ in custom associative memory chips for the pattern recognition. The FPGA-based track
⁴⁴⁷ fitter will perform a fast linear fit and the tracks are made available to the HLT. This
⁴⁴⁸ system will allow the use of tracks at much higher event rates in the HLT than is currently
⁴⁴⁹ affordable using CPU systems. However, the upgrade of the ATLAS trigger will not be
⁴⁵⁰ discussed any further.

⁴⁵¹ In the next sections the L1 and HLT will be briefly described.

⁴⁵² 2.3.1 Level 1 Trigger

⁴⁵³ The Level 1 Trigger identifies Regions of Interest (RoIs)³ and passes these to HLT which
⁴⁵⁴ will perform further investigations. Furthermore, in order to decide whether or not the
⁴⁵⁵ event processing will continue, L1 selection uses only information coming from some
⁴⁵⁶ parts of the detector to keep the input rate to a maximum of 100 kHz. L1 is implemented
⁴⁵⁷ in fast custom electronics to keep the latency⁴ below 2.5 μ s. Event data from other sub-
⁴⁵⁸ syststem are temporarily stored in memories whilst L1 decision is taken.

⁴⁵⁹ The L1 topological trigger (L1-Topo) [21] is feeded with energy and direction inform-
⁴⁶⁰ ation, about the objects found by the L1 calorimeter and the muon trigger, which will be
⁴⁶¹ processed by dedicated algorithms implemented in its own FPGAs. However, due to the
⁴⁶² 100 kHz read-out rate, not all the information collected by L1-Topo will be sent to the
⁴⁶³ HLT, but only part of it. In order to properly seed the ROI-guided HLT reconstruction,
⁴⁶⁴ specific objects in combination with the correct topological criteria must be employed.

⁴⁶⁵ 2.3.2 High-Level Trigger

⁴⁶⁶ The HLT is used to reduce the output rate down to 1 kHz and it has a \sim 200 ms average
⁴⁶⁷ decision time. Events that pass L1 trigger are then processed by the HLT using finer-
⁴⁶⁸ granularity calorimeter information, precision measurements from the MS and tracking
⁴⁶⁹ information from the ID. The HLT reconstruction can be run within RoIs identified at L1

³ $\eta - \phi$ regions where event features have been found by the L1 selection process.

⁴Time needed by an electric signal to get to the front-end electronics.

⁴⁷⁰ or a so-called full-scan on the full detector can be performed. The track reconstruction in
⁴⁷¹ the Inner Detector is an essential component of the trigger decision in the HLT and it will
⁴⁷² be discussed more in detail in Chapter 3

473

CHAPTER 3

474

475

The *b*-jet Trigger Signature in ATLAS

476

477 In this chapter the monitor and performance of the bottom-quark-initiated jet (*b*-jet) sig-
478 nature trigger, this being the author’s “technical/qualification task” to become a qualified
479 member of the experiment, will be discussed. The efficiencies of some of the Run 2 *b*-jet
480 triggers were evaluated using 3.8fb^{-1} of pp collisions data collected in 2015 with 25 ns
481 bunch-spacing.

482 The qualification task

483 3.1 Trigger Efficiency

484

CHAPTER 4

485

486

Event Simulation and Reconstruction

487

488 bla bla bla

489 4.1 Event Generation

490 bla bla

491 4.1.1 Parton Distribution Functions (PDFs)

492 bla bla bla

493 4.1.2 Matrix Element Calculation

494 bla bla bla

495 4.1.3 Parton Showers

496 bla bla bla

497 4.1.4 Hadronisation

498 bla bla bla

499 4.2 Detector Simulation

500 bla bla bla

501

CHAPTER 5

502

503 Stop searches in final states with jets and missing transverse energy

504

505

CHAPTER 6

506

Results and Statistical Intepreations

507

508

509 _____

510 Trigger

511 _____

512 bla vlas bla

513

514

Bibliography

515

- [1] C. Lefèvre, *The CERN accelerator complex.*, <http://cds.cern.ch/record/1260465>.
- [2] ATLAS Collaboration, *The ATLAS experiment at the CERN Large Hadron Collider*, Journal of Instrumentation **3** no. 08, (2008) S08003.
<http://stacks.iop.org/1748-0221/3/i=08/a=S08003>.
- [3] A. Collaboration, *Performance of the ATLAS Trigger System in 2015*, Eur. Phys. J. **C77** (2017), arXiv:1611.09661 [hep-ex].
- [4] M. Herrero, *The Standard Model.*, <https://arxiv.org/abs/hep-ph/9812242>.
- [5] ATLAS Collaboration, *Observation of a New Particle in the Search for the Standard Model Higgs Boson with the ATLAS Detector at the LHC*, Phys.Lett. **B716** (2012), arXiv:1207.7214 [hep-ex].
- [6] CMS Collaboration, *Observation of a new boson at a mass of 125 GeV with the CMS experiment at the LHC*, Phys.Lett. **B716** (2012), arXiv:1207.7235 [hep-ex].
- [7] K. A. Olive at al. (Particle Data Group), *Review of Particle Physics*, Chin.Phys. C **38(9)** (2014).
- [8] J.M. Jowett, M. Schaumann, R. Alemany, R. Bruce, M. Giovannozzi, P. Hermes, W. Hofle, M. Lamont, T. Mertens, S. Redaelli, J. Uythoven, J. Wenninger, *The 2015 Heavy-Ion Run of the LHC*,
<http://accelconf.web.cern.ch/accelconf/ipac2016/papers/tupmw027.pdf>.
- [9] O. S. Brüning, P. Collier, P. Lebrun, S. Myers, R. Ostojic, J. Poole and P. Proudlock, *LHC Design Report*, <https://cds.cern.ch/record/782076>.

- 536 [10] CMS Collaboration, *The CMS experiment at the CERN LHC*, Journal of
 537 Instrumentation **3** no. 08, (2008) S08004.
 538 <http://stacks.iop.org/1748-0221/3/i=08/a=S08004>.
- 539 [11] LHCb Collaboration, et. al, *The LHCb Detector at the LHC*, JINST (2008).
- 540 [12] ALICE Collaboration, *The ALICE experiment at the CERN LHC*, Journal of
 541 Instrumentation **3** no. 08, (2008) S08002.
 542 <http://stacks.iop.org/1748-0221/3/i=08/a=S08002>.
- 543 [13] A. Yamamoto, Y. Makida, R. Ruber, Y. Doi, T. Haruyama, F. Haug, H. ten Kate,
 544 M. Kawai, T. Kondo, Y. Kondo, J. Metselaar, S. Mizumaki, G. Olesen, O. Pavlov,
 545 S. Ravat, E. Sbrissa, K. Tanaka, T. Taylor, and H. Yamaoka, *The ATLAS central*
 546 *solenoid*, Nuclear Instruments and Methods in Physics Research Section A:
 547 Accelerators, Spectrometers, Detectors and Associated Equipment **584** no. 1, (2008)
 548 53 – 74.
 549 <http://www.sciencedirect.com/science/article/pii/S0168900207020414>.
- 550 [14] ATLAS Collaboration, *The ATLAS Inner Detector commissioning and calibration*, Eur.
 551 Phys. JC**70**, arXiv:1004.5293.
- 552 [15] ATLAS Collaboration, *ATLAS Insertable B-Layer Technical Design Report*,
 553 <https://cds.cern.ch/record/1291633>.
- 554 [16] G. A. et al., *ATLAS pixel detector electronics and sensors*, Journal of Instrumentation **3**
 555 no. 07, (2008) P07007. <http://stacks.iop.org/1748-0221/3/i=07/a=P07007>.
- 556 [17] A. Bingül, *The ATLAS TRT and its Performance at LHC*, Journal of Physics:
 557 Conference Series **347** no. 1, (2012) 012025.
 558 <http://iopscience.iop.org/article/10.1088/1742-6596/347/1/012025/meta>.
- 559 [18] ATLAS Collaboration, *ATLAS liquid-argon calorimeter: Technical Design Report*,
 560 <https://cds.cern.ch/record/331061>.
- 561 [19] ATLAS Collaboration, *ATLAS muon spectrometer: Technical design report*,
 562 <https://cds.cern.ch/record/331068>.
- 563 [20] ATLAS Collaboration, *Fast TracKer (FTK) Technical Design Report*,
 564 <https://cds.cern.ch/record/1552953>.

-
- 565 [21] E. Simoni, *The Topological Processor for the future ATLAS Level-1 Trigger: from design to*
566 *commissioning*, arXiv:1406.4316.